AUTHOR(S)
Aye, M. M., Rivasto, E., Huhtinen, H., & Paturi, P.

TITLE
Enhanced Critical Current Density in Heterostructural YBCO/Ca-Doped YBCO Multilayers

YEAR
2024

DOI
10.1021/acs.cgd.4c00200

CITATION
Aye, M. M., Rivasto, E., Huhtinen, H., & Paturi, P. (2024). *Enhanced Critical Current Density in Heterostructural YBCO/Ca-Doped YBCO Multilayers*. Crystal Growth & Design, 24(11), 4545–4555.
https://doi.org/10.1021/acs.cgd.4c00200

VERSION
Accepted Manuscript

Enhanced critical current density in heterostructural YBCO/Ca-doped YBCO multilayers

Moe Moe Aye,[*,†,‡] Elmeri Rivasto,[†,¶] Hannu Huhtinen,[†] and Petriina Paturi[†]

†*Wihuri Physical Laboratory, Department of Physics and Astronomy, University of Turku, 20014 Turku, Finland*

‡*University of Turku Graduate School (UTUGS), University of Turku, 20014 Turku, Finland*

¶*Current address: CP3-Origins, University of Southern Denmark, Campusvej 55, 5230 Odense M, Denmark*

E-mail: moe.m.aye@utu.fi

Abstract

We conducted experiments involving BZO-added YBCO/Ca-doped YBCO heterostructures with varying layer numbers to investigate the role of Ca-doping and the mechanism behind the enhanced J_c. Our findings reveal that the inclusion of Ca-doped layers enhances the quality of the YBCO matrix within the BZO-added layer by reducing microstrain and the formation of other crystalline defects, while also optimizing the oxygen content of YBCO with increasing layer number. These structural improvements lead to a significant increase in self-field $J_c(0)$, which is also observed to correspond to an increase in in-field $J_c(B)$ without directly impacting flux pinning. The remarkable enhancement in J_c at 65 K, can be explained by a theoretical model, where the improvement in J_c at high temperatures is attributed to the more coherent interface between the

BZO nanorods and the YBCO matrix. Therefore, we conclude that the overall enhancement of J_c in the Ca-doped heterostructures is attributed to the improved crystalline structure rather than enhanced flux pinning.

Keywords: YBCO, heterostructural film, Ca-doping, crystalline quality, self-field critical current density.

Introduction

The incorporation of artificial pinning centers (APCs) into high-temperature superconductor (HTS) films, using secondary non-superconductive additives, has been shown to significantly enhance in-field pinning and exhibit a pronounced anisotropy in the critical current angular dependence. This development positions APC-doped HTS as a highly promising choice for a wide range of power applications. Undoubtedly, $YBa_2Cu_3O_{6+x}$ (YBCO) stands out as the leading material for superconducting coated conductors in power applications due to its inherent ability to sustain exceptional current-carrying capacity, even in very high magnetic fields. Furthermore, the utilization of APCs holds the potential for further performance enhancements.

The integration of columnar structures created by secondary phases such as $BaZrO_3$ (BZO),[1] $BaSnO_3$ (BSO),[2,3] and $BaHfO_3$ (BHO)[4] into *c*-oriented epitaxial YBCO films is associated with strong pinning effects that significantly enhance the in-field critical current density $J_c(B)$ when the magnetic field aligns with the columns' axis. The influence of the strain field on YBCO with a secondary phase has been found crucial in determining the configuration of the secondary phase.[5,6] Furthermore, the double perovskite-like BYTO and BYNO, either individually or combined as $Ba_2Y(Nb/Ta)O_6$ (BYNTO), exhibit strong vortex pinning efficacy across a broad temperature and magnetic field range, offering efficient solutions for high-quality coated conductors, particularly in high fields.[7,8] Among the secondary phase perovskites, chemically and structurally compatible BZO is currently the most commonly used material for creating nanoscale pinning centers within the YBCO lattice. However, achieving optimal pinning efficiency poses a formidable challenge due to the high defect density at the semi-coherent BZO 1D-APC/YBCO interface caused by a significant lattice mismatch of approximately 9%.[9–11] Furthermore, the presence of substantial strain not only affects the growth of APCs but also degrades the superconducting performance of the YBCO matrix. This major obstacle hampers flux pinning and ultimately compromises the attainment of high J_c values in YBCO.[12–15]

To achieve optimal performance in high magnetic fields, it is essential to strike a perfect balance between $J_c(0)$ and $J_c(B)$ during the optimization of J_c. Thus, the persistent challenge in the field of high-temperature superconductors (HTS) lies in finding the ideal equilibrium between increased isotropic flux pinning and the avoidance of superconductivity loss. Simultaneously, it is necessary to approach the depairing current and attain sufficiently high $J_c(0)$ levels. Studies on multilayered YBCO films, incorporating different types of layers such as YBCO with secondary-phase materials,[16–21] APC-added YBCO,[13,22–24] and multilayers with varying APC-added YBCO,[25] have yielded promising results. These studies have not only shown a significant increase in J_c and in-plane pinning forces, particularly in high magnetic fields, but have also presented a viable approach for achieving the required film thickness in coated conductor technology.[19,23,26–28] Furthermore, recent research has revealed that partially substituting Ca for Y in YBCO, along with incorporating Ca-doped YBCO and YBCO into heterostructural multilayer films can considerably enhance J_c in films with low angle grain boundaries.[29,30] Like Ca-additions, incorporating Ag-additions in a multilayered configuration within YBCO films has demonstrated improved microstructural transparency, promoting supercurrent flow and resulting in a notable increase in J_c, particularly at relatively low fields.[31] Additionally, the introduction of a Ca-doped YBCO spacer layer to a BZO-doped YBCO layer can effectively improve the formation of a coherent BZO 1D-APC/YBCO interface by mitigating the lattice mismatch between BZO and YBCO.[32]

The objective of this study is to achieve the optimal equilibrium between $J_c(0)$ and $J_c(B)$ during the optimization of J_c. To accomplish this, we have fabricated multilayer structures with varying thicknesses by alternately depositing layers of BZO-doped YBCO and Ca-doped YBCO. Through a comprehensive analysis of the structural, magnetic, and resistive properties, we compare and discuss the characteristics of these multilayer structures in relation to single-layer films of BZO-doped YBCO.

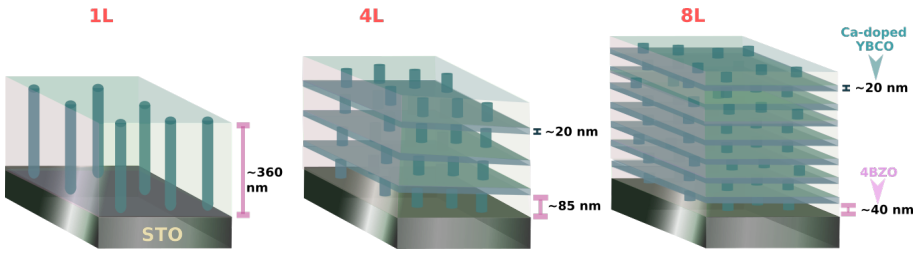

Figure 1: Two types of multilayer YBCO thin films (hereafter 4L, and 8L respectively) with alternating YBCO + 4%BZO and 30% Ca-doped YBCO with different thicknesses. A single layer film of YBCO + 4%BZO (1L) was deposited for comparison.

Experimental details

Multilayer films comprising heterolayers of 4 wt.% BZO-doped YBCO and 30 wt.% Ca-doped YBCO were deposited on $SrTiO_3$ (100) single crystal substrates using the pulsed laser deposition (PLD) technique. The multilayer structures consisted of 4 and 8 layers of BZO-doped YBCO (4L and 8L), with approximately 20 nm thickness of Ca-doped YBCO layers deposited between them, as illustrated in Fig. 1. The total thickness of BZO-doped YBCO was maintained at around 360 nm throughout the deposition. For comparison, a single layer of BZO-doped YBCO (1L) was also prepared. The material was ablated from the targets using a XeCl excimer laser (λ = 308 nm) with a laser energy density of 1.3 Jcm^{-2} and a repetition rate of 5 Hz. The ablation took place in a vacuum chamber with a pressure of 0.17 Torr. Sequential deposition of each layer was achieved by changing the PLD target *in situ*.[20] The substrate temperature was maintained at a constant 750 °C during deposition, and the films were post-annealed in an oxygen environment at 750 Torr for 10 min before being cooled to room temperature. Further details regarding the PLD system and deposition parameters can be found elsewhere.[33]

X-ray diffraction (XRD) measurements were conducted using a Philips Empyrean system to investigate the detailed structural properties, including in-plane and out-of-plane crystallographic characteristics of the deposited films. For high-resolution transmission electron microscopy (HRTEM), a JEOL JEM-2200FS electron microscope equipped with a 200 kV

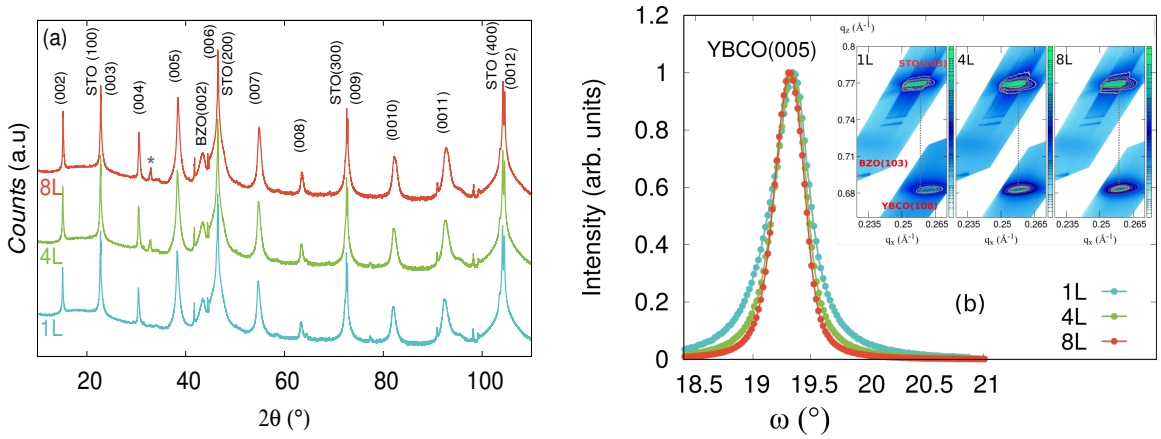

Figure 2: (a)Room temperature x-ray 2-θ diffractograms of a single layer 1L and multilayer 4L and 8L films, the gray star symbol denotes minor peak linked to the reflection of YBCO (110)-oriented grains. (b) The normalized XRD rocking curves (ω-scans) of the YBCO(005) peaks (the main panel) and the insets show the reciprocal space mapping (RSM) of the films.

field emission gun (FEG) and an in-column energy filter (Omega filter) was employed. Additionally, a probe-corrected scanning transmission electron microscope (STEM) utilizing high-angle annular dark-field imaging (HAADF STEM) was employed using a Titan 80–300 microscope operating at a voltage of 200 kV. The magnetic properties were measured using a Quantum Design Physical Property Measurement System (PPMS). The critical temperatures and critical current densities of the films were determined by analyzing ac magnetization curves and hysteresis loops based on the Bean model, which is suitable for rectangular films.[34] The angular dependence of the critical current density (J_c) was investigated using a standard four-probe method. Measurements were performed across a 0–360 ° angular range with 3 ° steps using the horizontal rotation option of the PPMS. The measurements were carried out at temperatures of 10 K, 40 K and 65 K in various magnetic fields.

Results

Effect of multilayering on the crystal quality

The x-ray diffractograms presented in Fig. 2(a) demonstrate the epitaxial growth of YBCO with a dominant orientation along the c-axis, as indicated by the intense $(00l)$ peaks. Additionally, the presence of minor peaks around $2\theta \approx 43^\circ$ confirms the formation of epitaxial BZO nanophase in all deposited films. The c-axis lattice parameters, obtained from (θ–2θ) scans of the (005) peaks, were found to be 11.724(2) Å and 11.719(3) Å for the 4L and 8L films, while the lattice constant of the 1L film was 11.728(1) Å. (Note that the numbers in the parentheses of c -axis lattice correspond to the standard deviations of the least significant digits of the parameter values.) Consistent with our previous observations,[33,35,36] the presence of BZO, with its larger lattice constant, results in tensile strain along the YBCO c-axis, leading to a slight extension of the c-axis in the doped samples compared to undoped YBCO (11.655(2) Å).[6] However, in the case of the multilayer films, the c lattice parameter is slightly shorter, and the YBCO (005) peak width in the 8L film is the narrowest. The 2D (2θ–ϕ) scan of the (102) peak confirmed that there is no systematic increase in the amount of a-axis oriented grains in any of the deposited films. To assess the in-plane and out-of-plane texture quality, ϕ-scan of YBCO (102) and BZO (110) peaks, as well as ω-scan of YBCO (005) and BZO (002) peaks, were performed. As shown in Table 1, the multilayered films exhibit excellent texture quality for both YBCO and BZO, with small full width at half maximum values of $\Delta\omega$ and $\Delta\phi$. Conversely, the widths of BZO peaks in the 1L film are noticeably larger compared to the multilayered films, which can be attributed to decreased in-plane and out-of-plane texture quality in the 1L film, likely due to enhanced strain and/or a higher number of defects in the YBCO. Furthermore, the lattice coherence length $r_c = 1/\pi \cdot d/l\Delta\omega$, calculated from the width of the (005) rocking curve,[37] is longer in the multilayered films, as shown in Fig. 2(b).

The findings of this study provide compelling evidence of the remarkable improvement

Table 1: Structural properties determined from the XRD measurements for multilayered of BZO doped YBCO samples 1L, 4L and 8L deposited on STO substrates: FWHM of YBCO $2\theta(005)$ peaks ($\Delta\theta_{005}$), FWHM of YBCO(005) rocking curve ($\Delta\omega_{005}$), FWHM of YBCO $\phi(102)$ peaks, $I(005)/I(004)$, the lattice coherence length (r_c), FWHM of BZO(002) rocking curve ($\Delta\omega_{002}$) and FWHM of BZO $\phi(110)$ peaks.

Film	$\Delta\theta_{005}(^\circ)$	$\Delta\omega_{005}(^\circ)$	$\Delta\phi_{102}(^\circ)$	$I(005)/I(004)$	r_c(nm)	$\Delta\omega_{002}(^\circ)$	$\Delta\phi_{110}(^\circ)$
1L	0.16	0.46	1.91	16.6	9.2	3.01	5.10
4L	0.16	0.45	1.94	14.3	9.5	2.85	4.97
8L	0.15	0.35	1.89	12.9	12.1	2.72	4.81

in both in-plane and out-of-plane crystallographic quality in the multilayered films, with the 8L film demonstrating exceptional enhancements. To investigate the strain effect on the film in more detail, x-ray reciprocal space map (RSM) analysis was conducted, and the results are shown in the inset of Fig. 2(b). The observed three main peaks, namely YBCO (108), STO (103), and BZO (103), indicate the orientation relationship of the film. These plots also enable the simultaneous determination of the in-plane and out-of-plane lattice parameters from the components of the scattering vector q of the selected (hkl) XRD reflection. The lattice constant values obtained from RSM scans align well with those from the (θ–2θ) scans. No significant variation is observed in the lateral and transverse directions (along the q_x and q_z directions) in the multilayered film, indicating a lack of increased disorder within the ab-planes and the c-axis. This suggests that the deposited films exhibit highly epitaxial growth. In contrast, the lateral direction (q_x) is observed to be shifted to a higher value in the 1L film compared to the multilayer films. A careful analysis of the figure reveals that this shift of the q_x component in the 1L film indicates its partially relaxed state, whereas the almost exact q_x match with the STO (103) peak in the multilayered films provides evidence of the coherent growth of the YBCO matrix. As concluded in Table 1, the intensity ratio of the (005) and (004) reflections is clearly decreased by multilayering, indicating that Ca doping may decrease the ratio or it can be related to decreased oxygen deficiency δ and thus increased average oxygen concentration of YBCO.[38]

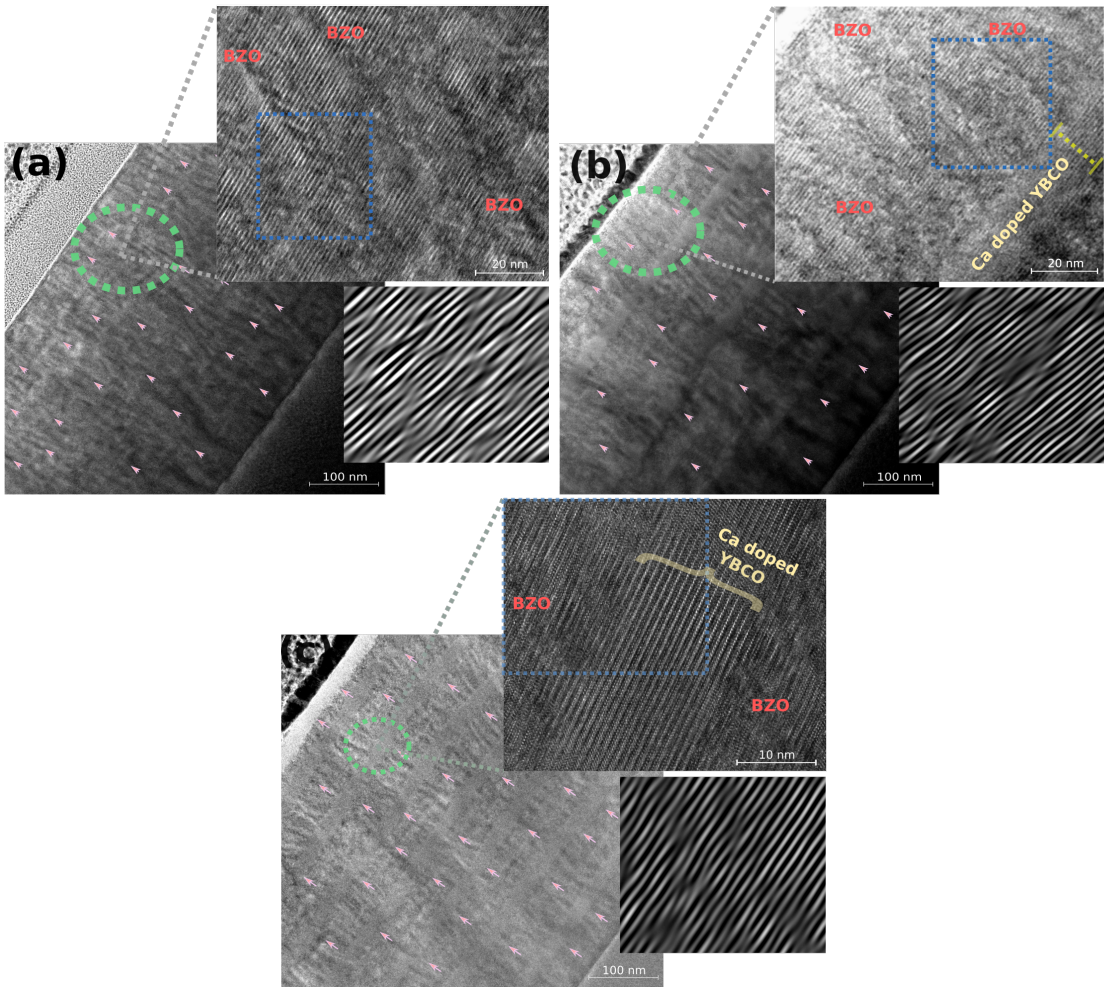

Figure 3: Cross-sectional STEM images of 1L (a), 4L (b) and 8L (c) films. The enlarged images indicated by the green circle and the FFT-filtered images from the blue square area of enlarged images shown on the right side bottom show the formation of the BZO nanorods, and the structural distortion together with the existence of misfit dislocations at the YBCO/BZO interfaces.

To investigate the distribution of the BZO secondary phase in the YBCO matrix and the associated defects caused by the dopant structures, STEM studies were conducted on all the films. Fig. 3(a-c) displays cross-sectional STEM images of the 1L, 4L, and 8L films. It is evident that BZO nanorods with a diameter of 6–8 nm are embedded in the YBCO matrix, and the vertically aligned growth of the BZO nanorods throughout the respective film layer thickness is observed in all deposited films. In 1L and 4L films, the average spacing between nanorods, estimated from STEM images, is ≈19 nm, whereas in the 8L film, it is

≈18 nm. The interfaces between the layers are barely distinguishable at the crystal lattice layer scale (enlargements in Fig. 3(a-c)). The hetero-multilayered structure of the films directly affects the length of the nanorods. The 4L and 8L films exhibit shorter nanorods of approximately 55 nm and 30 nm, respectively, compared to the 1L film, which has the longest nanorod length of approximately 85 nm. The enlarged images of the deposited film reveal the presence of lattice disorder and defects, including stacking faults and dislocations, uniformly across all films due to strain. Additionally, localized dislocation-like contrast can be observed along the interface between BZO and YBCO through the inversed fast Fourier transform (IFFT) image shown in the inset of the figure. As observed in the IFFT figures, the multilayered films exhibit a considerable number of dislocations and the formation of defects at the interfaces, although their quantity appears to be significantly lower compared to the single-layer film. Based on the structural results, it can be concluded that the multilayered films on averages exhibit lower lattice distortion induced by strain and accompanying defect density and thus improved crystallinity, which may lead to an improved coherence at the interface between YBCO and BZO.

Improvement of critical current density from magnetization measurements

The YBCO films, whether single or multilayered, exhibited nearly identical onset critical temperature ($T_{\mathrm{c,onset}}$) of ≈ 89 K when analyzed via resistive temperature dependencies, even with the integration of extra Ca-doped YBCO layers in a multilayer configuration, as seen in the inset figure of Fig. 4(d). However, the 1L film displayed a wider magnetically measured ΔT_{c} of 3.4 K compared to the multilayered films, where the ΔT_{c} values were 2.6 K and 2.1 K for the 4L and 8L films, respectively.

The smaller ΔT_{c} in the multilayered architecture can be attributed to increased crystalline quality, in contrast to the broader ΔT_{c} observed in the single-layer film, which confirms our earlier discussion on the deformation of the YBCO matrix structure. The remarkable

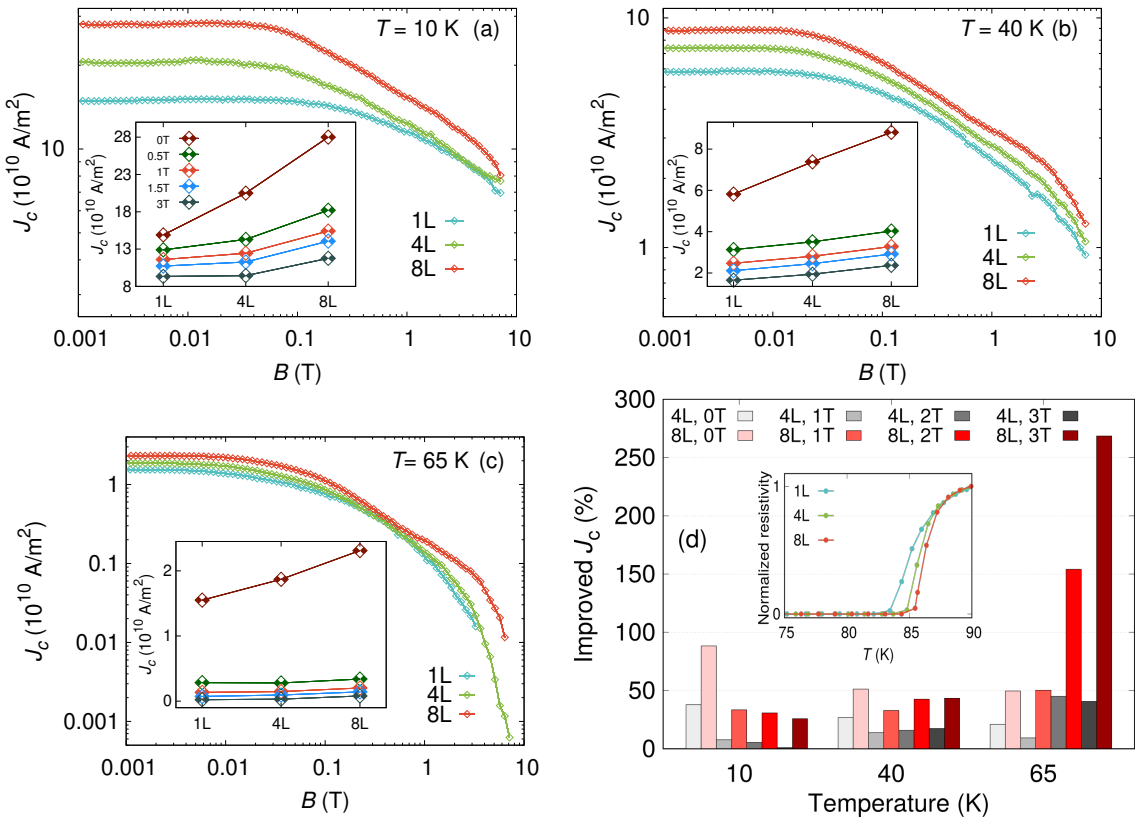

Figure 4: Magnetic field dependencies of J_c determined from the hysteresis loops measured at 10 K (a) 40 K (b) and 65 K (c) for 1L, 4L and 8L films. The insets show the J_c behaviour measured at different magnetic fields (B = 0, 0.5, 1, 1.5 and 3 T) when increasing the number of YBCO layers from 1L to 8L. (d) The improved J_c in multilayered films at different temperatures when compared to the J_c values of 1L. The inset figure depicts a graph of normalized resistivity versus temperature.

consistency of T_c and the smaller ΔT_c values across the hetero-multilayered YBCO films suggests that processing conditions had an impact on their superconducting properties, due to the effective enhancement of grain boundary coupling through Ca-doping, which resulted in a reduction in ΔT_c of these films. Hence, the lattice healing induced by Ca-doping is the key factor behind the improved performance of the multilayered films, as demonstrated by the XRD data showing a notable increase in r_c and a significant reduction in peak widths.

The critical current density as a function of magnetic field at 10 K, 40 K, and 65 K, calculated from the openings of the measured hysteresis loops using the Bean critical state model, is presented in Fig. 4(a-c). Remarkably, the multilayer films consistently exhibit

higher J_c compared to the single-layer film across all studied magnetic fields and temperature ranges, as seen in the inset figure of Fig. 4(a-c). The similarity in the behaviour of J_c in the multilayer films suggests that the nature of the pinning sites is likely the same. However, the decrease in $J_c(B)$ observed in the multilayered films is slightly faster than in 1L. This result can be attributed to the inclusion of nanorods in the deposited film architecture, where segmented nanorods formed by the hetero-multilayered structure slightly reduce correlated pinning.[25,39–41] Notably, the single-layer film exhibits a strong c-axis pinning and a weak field dependence of J_c, despite having a lower absolute J_c compared to the multilayered films. This is due to strongly correlated pinning by the more extended nanorod inclusions.

The lowest J_c observed in the 1L film across all temperatures and fields can be attributed to the poorer structural quality of the YBCO matrix caused by the presence of numerous pinning sites. This is supported by the accommodation field (B^*), denoting the critical magnetic field strength where the transition shifts from individual to collective vortex pinning.[42] The value of B^*, representing the upper limit of low-field plateau of $J_c(B)$, is determined based on the criterion $J_c(B)/J_c(0) = 0.9$.[33,43] At 10 K, the higher B^* value of 367 mT in 1L when compared with the values of 105 mT and 103 mT in films 4L and 8L attributed to the formation of greater number of individual nanoscale defects. Conversely, the decrease in B^* values observed in the multilayered films can be confidently attributed to the gradual healing of the lattice with thinner layers, which ultimately reduces the number of available pinning sites. Moreover, the slightly smaller α-values observed in the multilayer films, -0.22 and -0.23 for 4L and 8L when compared to -0.19 of 1L, as calculated from the decay of $J_c(T, B) = A(T)B^{\alpha}$ with the power-law, can be effectively attributed to the reduction in nanorod length,[13,40] resulting from decreasing layer thickness. Furthermore, the behaviour of the pinning force strongly depends on the temperature in magnetic fields higher than the matching field which is estimated from nanorod spacings of the TEM images to be ≈6 T for 1L and 4L and ≈7 T for 8L. As can be seen in Fig. 4(b-c), a slight upturn in the $J_c(B)$ curves around 1 T is observed in multilayer films, particularly in the 8L at temperatures 40 K

and 65 K. This can be explained by the presence of strong pinning centers (such as very coherent nanorods within 8L sample), where the vortex-vortex interactions enable some of the vortices to get trapped outside the nanorods. This is possible when several strongly pinned vortices form an energy minimum within the superconductor due to repulsive vortex-vortex interactions where a vortex can get trapped. This effect can take place in a rather narrow field range, since one has to have i) enough vortices to enable the outside nanorod pinning but ii) not too many vortices so that all of them can get effectively pinned.[44]

Figure 4(d) illustrates the improved percentage of J_c at different magnetic fields (0, 1, 2, and 3 T) observed in the multilayered films. It is evident that the multilayered films exhibit a remarkable enhancement in J_c across varying magnetic fields and at low temperature the improved in field J_c would be mainly related to significant increase of $J_c(0)$ in multilayered films. However, when the magnetic field exceeds 1 T ($B > 1$ T), there is a notable and significant enhancement in the J_c observed in the 8L film as the temperature is increased to 65 K. This intriguing result suggests that the 8ML film is particularly responsive to changes in temperature, and it exhibits a slower decline in J_c as temperature rises, when compared to the 1L film. This disparity in the behaviour of J_c with temperature serves as compelling evidence for the effectiveness of pinning mechanisms in multilayered films, especially at higher temperatures. This finding aligns with the recent theoretical model[45] which emphasizes the increasing efficacy of pinning centers with rising temperature. We will explore this issue further in the discussion section.

Angular dependence of critical current density

To conduct a comprehensive analysis of the shape and anisotropy of J_c as a function of angle (θ), we measured $J_c(\theta)$ curves at magnetic fields of 2 T, 4 T, and 8 T for temperatures of 10 K, 40 K and 65 K. However, since we observed similar behaviour across the entire magnetic field range and at 10 K and 40 K temperatures, we focus our attention on the results obtained at the highest field of 8 T and temperatures of 40 K and 65 K. Figure 5 illustrates the presence

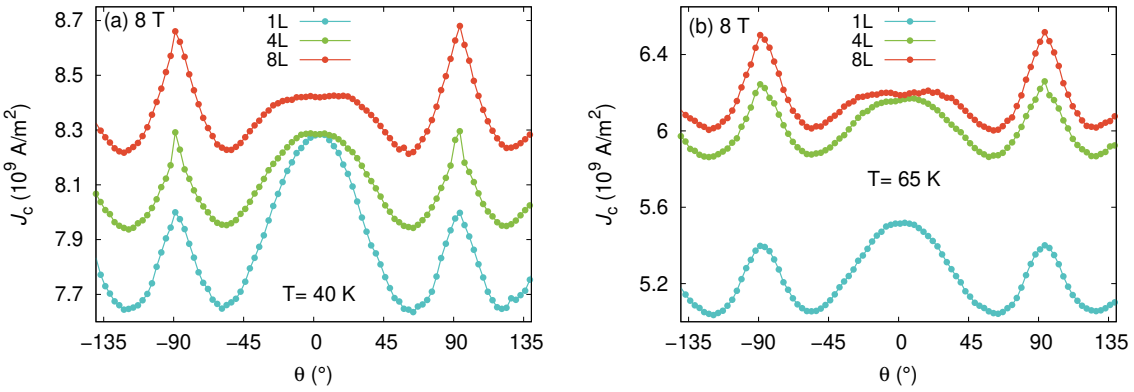

Figure 5: The angular dependencies of J_c measured in 8 T field at temperatures 40 K (a) and 65 K (b) for films 1L, 4L and 8L. The angles θ = -90° and 90° correspond to the *ab*-plane and θ = 0° the YBCO *c*-axis.

of distinct peaks along the *c*-axis in the $J_c(\theta)$ curve, providing evidence for the existence of a network composed of continuous nanorod-type APCs.[46,47] Notably, the multilayer films exhibit higher J_c values across the entire angular range. However, it is observed in transport measurements that the absolute J_c values are lower compared to those from magnetic measurements, a phenomenon attributed to the chosen voltage criterion and variations in the *n*-value, especially notable under high-temperature and magnetic field conditions.[48] At 40 K and in 8 T field, a noticeable difference can be observed in the $J_c(\theta)$ curves between the films. In the 1L film, the relatively narrow and intense *c*-axis peak can be qualitatively explained by the alignment of nanorods along the *c*-axis. Previous observations have also noted the presence of numerous edge dislocations around the BZO nanorod, which could accommodate an increased number of vortices at high fields, thereby narrowing the *c*-axis peak while intensifying it.[36,49] The multilayered films exhibit a sharper J_c peak along the *ab*-plane, which, together with the broadening of the *c*-axis peak and its double peak structure, can be attributed to enhanced pinning parallel to the *ab*-plane or the presence of shortened and tilted nanocolumns, as suggested previously.[50]

As shown in Figure 5(b), there is no significant difference in the shape of $J_c(\theta)$ when the temperature is increased to 65 K. However, the multilayered films exhibit remarkably higher

absolute J_c compared to the single-layer 1L film. This improvement can be attributed to the significantly enhanced pinning performance of the multilayered films at high temperatures, which contains a greater number of effective pinning centers. These results indicate the more intricate structural response of these films under high magnetic fields. The findings presented in this study align with earlier research on multilayer structures, demonstrating a consistent trend in the variation of $J_c(\theta)$ along the c-axis and in the vicinity of the ab-direction. The increased sharpness and strength of the ab-peaks observed in the multilayered films, achieved by decreasing the layer thickness while increasing their number, are strongly associated with a reduced intensity of the c-axis peaks, as discussed in previous studies.[21,23,25,51–53]

Discussion

Mechanisms behind improved self-field J_c with Ca-doped intermediate layers

To comprehend the potential mechanisms underlying the enhancement of the self-field critical current density, we have categorized this matter into three phenomena substantiated by our experimental findings: (i) enhanced crystalline growth through the interruption of the growth process via a multilayer structure, (ii) the impact of lattice mismatch and altered growth at the interface of the Ca-doped YBCO layer, and (iii) oxygen diffusion into the altered environment surrounding the BZO nanorods.

Previously, we have both experimentally and theoretically determined that the crystalline quality of YBCO thin films can be enhanced through the use of multilayering (Fig. 6(a)). This, in turn, extends the electron mean free path and consequently, the self-field $J_c(0)$.[54–56] Utilizing a multilayer structure allows for precise control over critical factors such as uniform and non-uniform strain relaxation, as well as the formation of dislocations and other defects in layers with constrained thicknesses. This approach offers the opportunity to increase the overall thickness of the film while maintaining improved crystalline properties. The

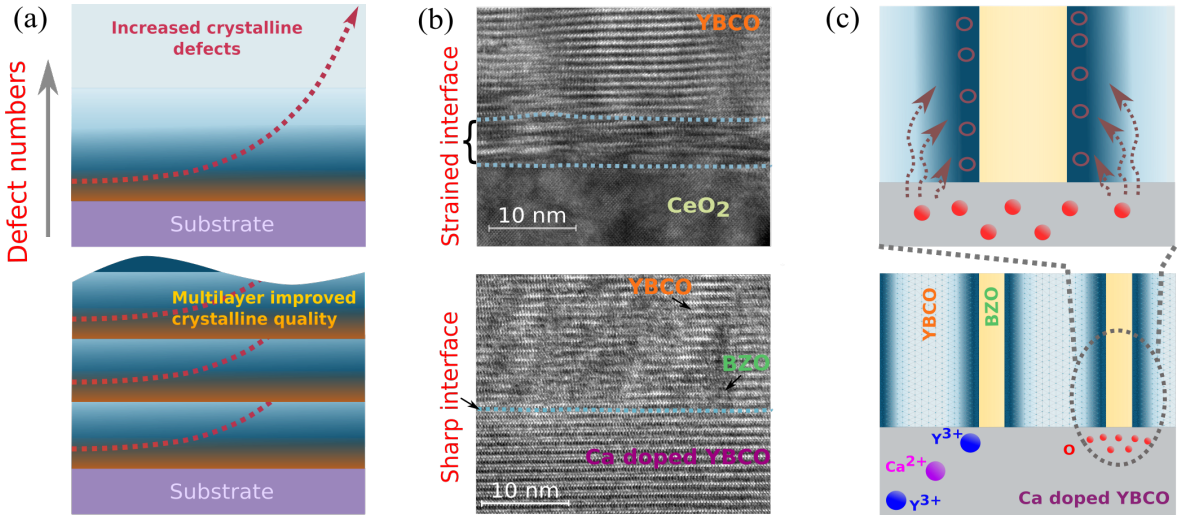

Figure 6: Schematic illustration of the mechanisms, which may lead to improved crystalline quality and decreased number of dislocations and YBCO lattice distortions, and thus result in increased self-field $J_c(0)$. (a) represent the effect of multilayering, where strain relaxation, increasing number of lattice distortions and critical thickness play a key role, the orange color indicates the strained regions at the substrate/film interface, (b) the effect of lattice mismatch and the epitaxial growth at the layer interface, when compared the effect of Ca-doped YBCO layer with the interface of CeO_2 layer, and (c) diffusion of the mobile oxygen atoms from the equilibrium state in Ca-doped YBCO layer to compensate for the oxygen vacancies formed around the BZO nanorods by strain.

implementation of a multilayer structure can be achieved, for instance, by incorporating a CeO_2 interlayer or by periodically interrupting the film growth through sequential vacuum treatment. These techniques have been shown to enhance the crystalline quality of each sublayer, reducing the likelihood of defect formation in subsequent deposition intervals.[55,56]

Secondly, the underlying Ca-doped YBCO layer serves as an ideal foundation for the 4% BZO-doped YBCO layer. Notably, Ca-doped YBCO exhibits average in-plane and out-of-plane lattice parameters ($a = 3.83$ Å, $b = 3.88$ Å, and $c = 11.71$ Å) that closely match those of BZO-doped YBCO. This match is much closer than what is observed with undoped YBCO. Consequently, this significantly minimizes the strain induced by the layer below. This is evident in earlier shown TEM images (see Fig. 3(b-c)), where the growth of BZO-doped YBCO directly above the Ca-doped YBCO layer occurs smoothly, epitaxially through the interface, without the presence of any distorted layers next to it (Fig. 6(b)). In contrast, when for

example using a CeO_2 interlayer, a strained region several nanometers thick consistently forms above the CeO_2 interlayer.[56]

Finally, based on the literature, the partial substitution of Ca^{2+} ions at Y^{3+} sites in YBCO alters the carrier concentration and affects the transfer of charges from the CuO chains to the conducting CuO_2 planes.[57,58] The fixed charge is entirely offset by oxygen defects, resulting in a slightly reduced equilibrium oxygen content, which also contributes to a lower superconducting transition temperature.[59] However, various aliovalent atomic substitutions in YBCO have been found to increase the oxygen diffusion rate by up to a factor of 100.[57,58] Since it has been demonstrated that within the interface region, spanning a few nanometers between BZO nanorods and the YBCO matrix, substantial strain and misfit dislocations lead to an increase in oxygen vacancy concentration,[15,60] we can infer that thermodynamically driven mobile oxygen can readily migrate into these vacant sites (Fig. 6(c)). Consequently, this process modifies the distorted BZO/YBCO interface, bringing it closer to the optimal YBCO state. Moreover, research has demonstrated that Ca-doping up to 30% can elevate the self-field critical current densities in grain boundaries of both polycrystalline YBCO and YBCO superlattices and bilayers.[30,61] Such findings carry notable implications for coated conductor technology, where the influence of grain boundaries must be carefully considered.

Temperature dependent vortex pinning mechanisms

The high-field J_c of the 8L film with respect to the conventional 1L film increases in an exponential manner with temperature (Fig. 4), reaching over 250% improved J_c at 65 K. At the same time, the zero-field J_c improvement can be observed to decrease with temperature. These observations undeniably suggest that the underlying mechanism behind the superior high-field J_c of the 8L film is related to seemingly temperature dependent vortex pinning. The BZO nanorods within the Ca-doped films have been previously observed to have significantly more coherent BZO-YBCO interface when compared with the conventional films.[32]

The temperature dependence of vortex pinning has been considered to results from two

distinct mechanisms.[62,63] These include the *intrinsic effects* resulting directly from the temperature dependence of the penetration depth (λ) and coherence length (ξ) along with *thermal fluctuations* associated with random depinning of the vortices. These two mechanisms behave opposite to each other. The intrinsic effects increase the size of the vortex core as temperature is increased resulting in deeper pinning potentials of the lattice defects (see Eqs. (1)–(2) and below discussion). That is, intrinsic effects enhance the pinning of the vortices as a function of temperature. Note, that in the context of this work the intrinsic effects exclude all kinds of multi defect pinning. On the contrary to the intrinsic pinning, the thermal fluctuations inherently decrease vortex pinning efficiency at higher temperatures due to thermal unpinning of vortices. It should be further noted, that the $J_\mathrm{c}(B)$ is ultimately governed by the properties of the strong pinning centers within the superconductor and consequently the effects of vortex-vortex interactions, that are also the similar between the samples, can and will be neglected in the upcoming discussion.

The pinning potential associated with an ideally coherent columnar defect can be generally calculated as[62,63]

$$u(x_\mathrm{v}) \propto \epsilon_0(T) \cdot \int_0^R 1 - |\psi_\mathrm{v}(x - x_\mathrm{v})|^2 dx, \tag{1}$$

where $\epsilon_0(T) \propto \lambda(T)^{-2}$ is the characteristic pinning energy, R is the radius of the defect centered at $x = 0$ and $\psi_\mathrm{v}(x)$ is the spatially varying complex order parameter in the vicinity of the vortex core located at $x = x_\mathrm{v}$. The $\psi_\mathrm{v}(x)$ can be approximated as $\psi_\mathrm{v}(x) = \psi_{\mathrm{v},0}(x) \cdot \mathrm{e}^{i\theta}$, where θ is the phase of the complex valued wave function and[64]

$$\psi_{\mathrm{v},0}(x) = \frac{x}{(x^2 + 2 \cdot \xi(T)^2)^{1/2}}. \tag{2}$$

In the above equation the superconducting coherence length has temperature dependence $\xi(T) = \xi_0 \cdot (1 - T/T_\mathrm{c})^{-1/2}$ with $\xi_0 \approx 1.5\,\mathrm{nm}$, that is characteristic for YBCO. The previously introduced λ has similar temperature dependence with corresponding $\lambda_0 \approx 150\,\mathrm{nm}$ for YBCO.[65] The temperature dependence of intrinsic pinning ultimately results from $\xi(T)$ and

$\lambda(T)$. Note, that the presented model of a vortex remarkably differs from the simplistic, but still quite widely used, model where the dynamics of a vortex is determined by its core, that is considered to be a uniform region of diameter $2 \cdot \xi(T)$ where $\psi = 0$. The main difference between this *simplistic model* and the more *advanced model* used in this work (based on Eq. (2)[62–64]) is how one considers the temperature dependent size of the vortex. While the simplistic model explicitly assigns the vortex a certain size, this is not well defined in the advanced model used in this work. Instead, the advanced model results in increasing flatness of the $\psi_{\mathrm{v},0}(x)$ in the vicinity of its minimum point as the temperature is increased. This increasing flatness is then analogous to the increase of the core diameter as a function of temperature in the simplistic model.

While Eq. (1) holds for ideally coherent interfaces between the columnar defect and the superconducting matrix, it fails to take into account the existence of several experimentally observed structural deformations in the vicinity of the columnar defect, making the associated interface non-coherent. Most prominently, this includes the increased number of dislocations and oxygen vacancies located in the vicinity of the columnar defects, such as particularly observed for the 1L film in this work. The effects of such deformations on the depth of the pinning potential could be taken into account by introducing an effective radius R_{eff} to be used as the upper limit for integration in Eq. (1). However, the effects on the spatial shape of the pinning potential will still be neglected. The only plausible way to take these effects into account is to generalize Eq. (1) as

$$u(x_{\mathrm{v}}) \propto \epsilon_0(T) \cdot \int_{-\infty}^{+\infty} \chi(x) \cdot \left[1 - |\psi_{\mathrm{v}}(x - x_{\mathrm{v}})|^2\right] dx, \tag{3}$$

where we have introduced a dimensionless *form factor* $\chi(x)$ representing the spatial variation of magnetic permeability in the vicinity of a columnar defect. Following the two-fluid model of superconductivity, this can be related to the superconducting order parameter as $\chi(x) = 1 - |\psi(x)|^2$. Calculating the pinning potential thus becomes simply the matter of

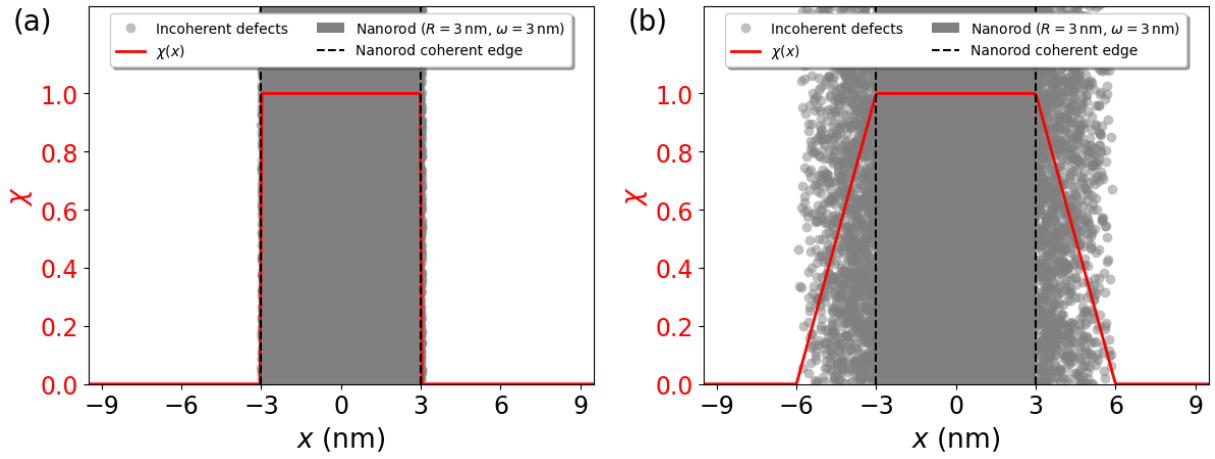

Figure 7: Schematic illustrations of how the form factor (∼magnetic permeability) (Eq. (4)) is considered to change in the vicinity of a 3 nm radius nanorod with (a) ideally coherent interface with $\omega \approx 0$ and (b) incoherent interface characterized by a width $\omega = 3$ nm over which the μ is degraded from its maximum value inside the nanorod down to zero within the ideal superconducting lattice.

approximating the $\chi(x)$ in the vicinity of a defect.

For the lack of better analytic function, the simplest way to associate $\chi(x)$ with the morphology of the columnar defects and the associated interface is to define it step-wise as (assuming that the center of a R-radius nanorod is located at $x = 0$)

$$\chi(x, R, \omega) = \begin{cases} 0 & \text{when } |x| \geq R + \omega \\ \frac{\chi_0}{\omega} \cdot x + \frac{\chi_0 \cdot (R+\omega)}{\omega} & \text{when } -(R+\omega) < x < -R \\ \chi_0 & \text{when } -R \leq x \leq R \\ -\frac{\chi_0}{\omega} \cdot x + \frac{\chi_0 \cdot (R+\omega)}{\omega} & \text{when } R < x < R + \omega \end{cases}, \tag{4}$$

where the parameter ω represents the distance over which the assumably temperature independent, form factor degrades from $\chi_0 = 1$ inside the nanorod to zero within the superconducting lattice. The ω is to be treated as a phenomenological parameter that is directly proportional to the coherence of the interface between nanorod and the superconductor. The correspondence between the nanorod-superconductor interface and the shape of $\chi(x)$ (Eq.

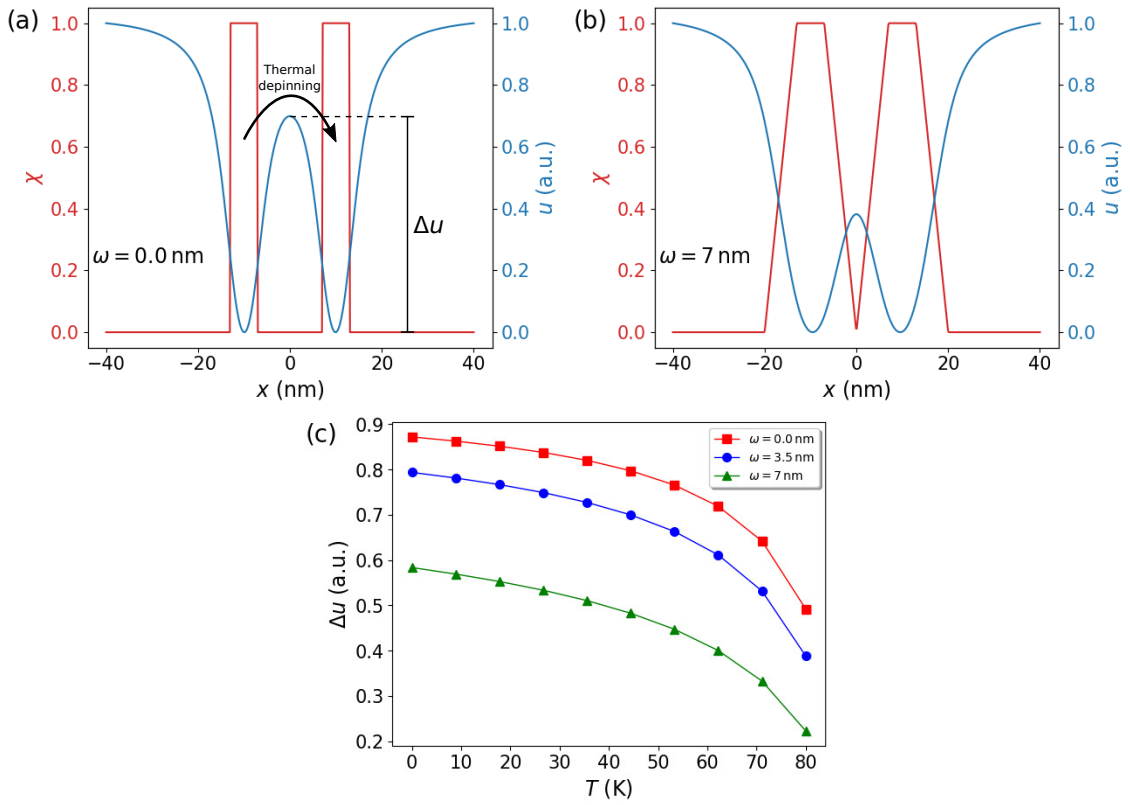

Figure 8: (a) The spatially varying form factor (red curve) for a system of two ideally coherent nanorods ($\omega = 0\,\mathrm{nm}$) and the associated pinning potential (blue curve) according to Eq. (3). The figure also illustrates the hopping potential (Δu) associated with thermal depinning of a vortex. (b) The same as previous but for incoherent nanorod interfaces ($\omega = 7\,\mathrm{nm} > 0$). (c) The calculated hopping potentials as a function of temperature for two nanorod systems associated with different interface coherence parameters (ω).

(4)) is schematically illustrated in Fig. 7(a)–(b). It should be further noted, that in the limit $\omega \to 0$, corresponding to ideally coherent interface, Eq. (3) becomes equivalent to Eq. (1).

Looking at Eq. (3) it becomes evident that the pinning potential gets deeper when ω is increased regardless of the temperature range. More intuitively, the increase of ω can be considered as an increase in the *effective radius* of the nanorod which consequently increases its pinning force. Naturally, this also improves the tolerance for thermal depinning of vortices. From these observations one can conclude that the experimentally observed increased pinning performance of the Ca-doped films cannot result from the pinning performance of individual vortices, but rather from their collective effect.

To illustrate this, consider a system of two nanorods with $R = 3\,\mathrm{nm}$ separated by a distance $s = 15\,\mathrm{nm}$ (edge-to-edge) based on the TEM measurements. The spatially varying $\mu(x)$ and the resulting pinning potentials for this particular system associated with $\omega = 0\,\mathrm{nm}$ and $\omega = 7\,\mathrm{nm}$ at $40\,\mathrm{K}$ temperature are presented in Figs. 8(a)–(b), respectively. One can observe that the potential hill between the nanorods (Δu) significantly decreases with ω. The Δu represents the hopping potential of the vortices associated with their thermal depinning. Given that the rate of the thermal depinning increases with temperature as $\propto \exp(-\Delta u/kT)$, one can conclude that the thermal depinning is significantly decreased for nanorods with more coherent interfaces, that is for small ω. Fig. 8(c) further illustrates the evolution of Δu with temperature for nanorods associated with $\omega = 0\,\mathrm{nm}$, $\omega = 3.5\,\mathrm{nm}$ and $\omega = 7\,\mathrm{nm}$. While these values for ω are arbitrary, without a direct link to quantitative structural measurements of the studied samples, we still consider their range very plausible for the associated physical systems. This is, at least to the extent that we can reliably conclude Δu significantly decreasing over the whole temperature range when the BZO-YBCO interface becomes more decoherent. This is seen in Fig. 8(c) as the perfectly coherent nanorods ($\omega = 0$) can be observed to be significantly higher over the full temperature range compared to other cases with higher ω. Consequently, the rate of thermal depinning, particularly at high temperature range, will be significantly lower for nanorods associated with improved interface coherence (small ω). This is in line with the experimental observations (Fig. 4(d)), where the Ca-doped films, associated with lower ω when compared with normal films, achieve by far the greatest J_c improvement particularly at the highest measured temperature of $65\,\mathrm{K}$.

In summary, the nanorods in the Ca-doped films can be assumed to have more coherent BZO-YBCO interface when compared with the conventional samples. This improved coherence of the nanorod-superconductor interface ultimately leads to better tolerance against thermal depinning of vortices, consequently improving the vortex dynamics limited J_c particularly at high temperature range.

Conclusions

In conclusion, our study focused on the investigation of enhanced crystalline quality and self-field critical current properties in YBCO and Ca-doped YBCO heterostructural multilayers. Through our experimental findings, we have uncovered significant improvements in both the structural and superconducting properties of these multilayers.

Regarding the structural properties, we observed a remarkable enhancement in crystalline quality, particularly in the in-plane and out-of-plane textures of both YBCO and BZO nanorods. This improvement was evidenced by the smaller x-ray diffraction peak widths, indicating reduced lattice distortion. Moreover, the hetero-multilayered films exhibited superior out-of-plane coherence, despite the shorter length of BZO nanorods. These findings suggest that the process of multilayering contributes to the overall reduction in lattice distortion. Moving on to the superconducting properties, we observed a substantial increase in the self-field critical current density due to the multilayering. Furthermore, the in-field properties, especially at high temperatures, demonstrated significant improvement. These enhancements indicate an improved crystalline structure of YBCO, facilitating the superior growth of BZO nanorods.

To explain the observed results of improved crystalline quality and increased self-field critical current densities, we have suggested three contributing mechanisms. Additionally, we have discussed the role of BZO nanorods and their effective contribution to the flux pinning at high temperatures. In summary, our findings pave the way for further advancements in the design and fabrication of high-performance superconducting materials for various applications.

ACKNOWLEDGEMENTS

The Jenny and Antti Wihuri Foundation and the University of Turku Graduate School are acknowledged for financial support.

References

(1) MacManus-Driscoll, J. L.; Foltyn, S. R.; Jia, Q. X.; Wang, H.; Serquis, A.; Civale, L.; Maiorov, B.; Hawley, M. E.; Maley, M. P.; Peterson, D. E. Strongly enhanced current densities in superconducting coated conductors of $YBa_2Cu_3O_{7-x}$ + $BaZrO_3$. *Nat. Mater.* **2004**, *3*, 439.

(2) Varanasi, C. V.; Barnes, P. N.; Burke, J.; Brunke, L.; Maartense, I.; Haugan, T. J.; Stinzianni, E. A.; Dunn, K. A.; Haldar, P. Flux pinning enhancement in $YBa_2Cu_3O_{7-x}$ films with $BaSnO_3$ nanoparticles. *Supercond. Sci. Technol.* **2006**, *19*, L37–L41.

(3) Varanasi, C. V.; Burke, J.; Brunke, L.; Wang, H.; Sumption, M.; Barnes, P. N. Enhancement and angular dependence of transport critical current density in pulsed laser deposited $YBa_2Cu_3O_{7-x}$+$BaSnO_3$ films in applied magnetic fields. *J. Appl. Phys.* **2007**, *102*, 063909:1–5.

(4) Tobita, H.; Notoh, K.; Higashikawa, K.; Inoue, M.; Kiss, T.; Kato, T.; Hirayama, T.; Yoshizumi, M.; Izumi, T.; Shiohara, Y. Fabrication of $BaHfO_3$ doped $Gd_1Ba_2Cu_3O_{7-\delta}$ coated conductors with the high I_c of 85 A/cm-w under 3 T at liquid nitrogen temperature (77 K). *Supercond. Sci. Technol.* **2012**, *25*, 062002.

(5) Wu, J.; Shi, J. Interactive modeling-synthesis- characterization approach towards controllable in situ self-assembly of artificial pinning centers in RE-123 films. *Supercond. Sci. Technol.* **2017**, *30*, 103002.

(6) Aye, M. M.; Rivasto, E.; Rijckaert, H.; Huhtinen, H.; Driessche, I. V.; Paturi, P. Controlled BZO Nanorod Growth and Improved Flux Pinning in YBCO Films Grown on Vicinal STO Substrates. *Cryst. Growth Des* **2023**, *23*, 7971–7981.

(7) Opherden, L.; Sieger, M.; Pahlke, P.; Hühne, R.; Schultz, L.; Meledin, A.; Tendeloo, G. V.; Nast, R.; Holzapfel, B.; Bianchetti, M.; MacManus-Driscoll, J. L.;

Hänisch, J. Large pinning forces and matching effects in $YBa_2Cu_3O_{7-\delta}$ thin films with $Ba_2Y(Nb/Ta)O_6$ nano-precipitates. *Scientific Reports* **2016**, *6*, 21188.

(8) Rizzo, F.; Augieri, A.; Armenio, A. A.; Galluzzi, V.; Mancini, A.; Pinto, V.; Rufoloni, A.; Vannozzi, A.; Bianchetti, M.; Kursumovic, A.; MacManus-Driscoll, J. L.; Meledin, A.; Tendeloo, G. V.; Celentano, G. Enhanced 77 K vortex-pinning in $YBa_2Cu_3O_{7-x}$ films with Ba_2YTaO_6 and mixed Ba_2YTaO_6 + Ba_2YNbO_6 nano-columnar inclusions with irreversibility field to 11 T. *APL Materials* **2016**, *4*, 061101.

(9) Wang, X.; Baca, F. J.; Emergo, R. L. S.; Wu, J. Z.; Haugan, T. J.; Barnes, P. N. Eliminating thickness dependence of critical current density in $YBa_2Cu_3O_{7-x}$ films with aligned $BaZrO_3$ nanorods. *J. Appl. Phys.* **2010**, *108*, 113911:1–5.

(10) Augieri, A.; Celentano, G.; Galluzzi, V.; Mancini, A.; Rufoloni, A.; Vannozzi, A.; Armenio, A. A.; Petrisor, T.; Ciontea, L.; Rubanov, S.; Silva, E.; Pompeo, N. Pinning analyses on epitaxial $YBa_2Cu_3O_{7-\delta}$ films with $BaZrO_3$ inclusions. *J. Appl. Phys.* **2010**, *108*, 063906.

(11) MacManus-Driscoll, J. L.; Foltyn, S. R.; Jia, Q. X.; Wang, H.; Serquis, A.; Civale, L.; Maiorov, B.; Hawley, M. E.; Maley, M. P.; Peterson, D. E. Strongly enhanced current densities in superconducting coated conductors of $YBa_2Cu_3O_{7-x}$+$BaZrO_3$. *Nat. Mater.* **2004**, *3*, 439–443.

(12) Foltyn, S. R.; Civale, L.; MacManus-Driscoll, J. L.; Jia, Q. X.; Maiorov, B.; Wang, H.; Maley, M. Materials science challenges for high-temperature superconducting wire. *Nat. Mater.* **2007**, *6*, 631.

(13) Ichinose, A.; Naoe, K.; Horide, T.; Matsumoto, K.; Kita, R.; Mukaida, M.; Yoshida, Y.; Horii, S. Microstructures and critical current densities of YBCO films containing structure-controlled $BaZrO_3$ nanorods. *Supercond. Sci. Technol.* **2007**, *20*, 1144–1150.

(14) Mele, P.; Matsumoto, K.; Horide, T.; Ichinose, A.; Mukaida, M.; Yoshida, Y.; Horii, S.; Kita, R. Ultra-high flux pinning properties of $BaMO_3$-doped $YBa_2Cu_3O_{7-x}$thin films (M = Zr, Sn). *Supercond. Sci. Technol.* **2008**, *21*, 032002.

(15) Cantoni, C.; Gao, Y.; Wee, S. H.; Specht, E. D.; Gazquez, J.; Meng, J.; Pennycook, S. J.; Goyal, A. Strain-driven oxygen deficiency in self-assembled, nanostructured, composite oxide films. *ACS Nano* **2011**, *5*, 4783–4789.

(16) Haugan, T.; Barnes, P. N.; Wheeler, R.; Meisenkothen, F.; Sumption, M. Addition of nanoparticle dispersions to enhance flux pinning of the $YBa_2Cu_3O_{7-x}$ superconductor. *Nature* **2004**, *430*, 867.

(17) Barnes, P. N.; Haugan, T. J.; Varanasi, C. V.; Campbell, T. A. Flux pinning behavior of incomplete multilayered lattice structures in YBCO. *Appl. Phys. Lett.* **2004**, *85*, 4088.

(18) Campbell, T. A.; Haugan, T. J.; Maartense, I.; Murphy, J.; Brunke, L.; Barnes, P. N. Flux pinning effects of Y_2O_3 nanoparticulate dispersions in multilayered YBCO thin films. *Physica C* **2005**, *423*, 1.

(19) Jia, Q. X.; Foltyn, S. R.; Arendt, P. N.; Smith, J. F. High-temperature superconducting thick films with enhanced supercurrent carrying capability. *Appl. Phys. Lett.* **2002**, *80*, 1601–1603.

(20) Huhtinen, H.; Schlesier, K.; Paturi, P. Growth and *c*-axis flux pinning of nanostructured YBCO/BZO multilayers. *Supercond. Sci. Technol.* **2009**, *22*, 075019:1–8.

(21) Haugan, T. J.; Barnes, P. N.; Campbell, T. A.; Pierce, N. A.; Baca, F. J.; Maartense, I. Flux Pinning of Y-Ba-Cu-O Films Doped With $BaZrO_3$ Nanoparticles by Multilayer and Single Target Methods. *IEEE T. Appl. Supercond.* **2007**, *17*, 3724.

(22) Kobayashi, H.; Yamada, Y.; Ibi, A.; Miyata, S.; Shiohara, Y.; Kato, T.; Hirayama, T. Investigation of in-field properties of YBCO multi-layer film on PLD/IBAD metal substrate. *Physica C* **2007**, *463–465*, 661–664.

(23) Kang, S.; Leonard, K. J.; Martim, P. M.; Li, J.; Goyal, A. Strong enhancements of flux pinning in YBCO multilayers with columnar defects comprised of self-assembled $BaZrO_3$ nanodots. *Supercond. Sci. Technol.* **2007**, *20*, 11.

(24) Matsumoto, K.; Tanaka, I.; Horide, T.; Mele, P.; Yoshida, Y.; Awaji, S. Irreversibility fields and critical current densities in strongly pinned $YBa_2Cu_3O_{7-x}$ films with $BaSnO_3$ nanorods: The influence of segmented $BaSnO_3$ nanorods. *J. Appl. Phys.* **2014**, *116*, 163903:1–7.

(25) Malmivirta, M.; Rijckaert, H.; Paasonen, V.; Huhtinen, H.; Hynninen, T.; Jha, R.; Awana, V. S.; Driessche, I. V.; Paturi, P. Enhanced flux pinning in YBCO multilayer films with BCO nanodots and segmented BZO nanorods. *Sci. Reports* **2017**, *7*, 14682:1–8.

(26) Pan, A. V.; Pysarenko, S. V.; Dou, S. X. Drastic improvement of surface structure and current-carrying ability in YBa_2 Cu_3O_7 films by introducing multilayered structure. *Appl. Phys. Lett.* **2006**, *88*, 232506.

(27) Pan, A. V.; Pysarenko, S. V.; Wexler, D.; Rubanov, S.; Ionescu, M.; Dou, S. X. Multilayered deposition and its role in the enhancement of $YBa_2Cu_3O_7$ film performance. *Physica C* **2007**, *460-462*, 1379.

(28) Foltyn, S. R.; Civale, L.; MacManus-Driscoll, J. L.; Jia, Q. X.; Maiorov, B.; Wang, H.; Maley, M. Materials science challenges for high-temperature superconducting wire. *Nat. Mater.* **2007**, *6*, 631–642.

(29) Song, X.; Daniels, G.; Feldmann, D. M.; Gurevich, A.; Larbalestier, D. Electromagnetic,

atomic structure and chemistry changes induced by Ca-doping of low-angle YBCO grain boundaries. *Nature Mat.* **2005**, *4*, 470–475.

(30) Hammerl, G.; Schmehl, A.; Schulz, R. R.; Goetz, B.; Bielefeldt, H.; Schneider, C. W.; Hilgenkamp, H.; Mannhart, J. Enhanced supercurrent density in polycrystalline $YBa_2Cu_3O_{7-\delta}$ at 77 K from calcium doping of grain boundaries. *Nature* **2000**, *407*, 162–164.

(31) Pan, A. V.; Pysarenko, S. V.; Wexler, D.; Rubanov, S.; Dou, S. X. Multilayering and Ag-doping for properties and performance enhancement in $YBa_2Cu_3O_7$ films. *IEEE T. Appl. Supercond.* **2007**, *17*, 3585.

(32) Ogunjimi, V.; Sebastian, M. A.; Zhang, D.; Gautam, B.; Jian, J.; Huang, J.; Zhang, Y.; Haugan, T.; Wang, H.; Wu, J. Enhancing magnetic pinning by $BaZrO_3$ nanorods forming coherent interface by strain-directed Ca-doping in $YBa_2Cu_3O_{7-x}$ nanocomposite films. *Supercond. Sci. Technol.* **2021**, *34*, 104002.

(33) Peurla, M.; Paturi, P.; Stepanov, Y. P.; Huhtinen, H.; Tse, Y. Y.; Bódi, A. C.; Raittila, J.; Laiho, R. Optimization of the $BaZrO_3$ concentration in YBCO films prepared by pulsed laser deposition. *Supercond. Sci. Technol.* **2006**, *19*, 767–771.

(34) Wiesinger, H. P.; Sauerzopf, F. M.; Weber, H. W. On the calculation of J_c from magnetization measurements on superconductors. *Physica C* **1992**, *203*, 121–128.

(35) Aye, M. M.; Rivasto, E.; Rijckaert, H.; Palonen, H.; Huhtinen, H.; Van Driessche, I.; Paturi, P. Optimized $BaZrO_3$ nanorod density in $YBa_2Cu_3O_{6+x}$ matrix for high field applications. *Supercond. Sci. Technol.* **2022**, *35*, 075006:1–10.

(36) Peurla, M.; Huhtinen, H.; Tse, Y. Y.; Raittila, J.; Paturi, P. Structural properties of YBCO thin films deposited from different kinds of targets. *IEEE T. Appl. Supercond.* **2007**, *17*, 3608–3611.

(37) Gauzzi, A.; Pavuna, D. Quantitative analysis of growth-induced reduction of long range lattice order in ion-beam sputtered $YBa_2Cu_3O_{6.9}$ films. *Appl. Phys. Lett.* **1995**, *66*, 1836–1838.

(38) Yeh, N. C.; Kriplani, U.; Jiang, W.; Reed, D. S.; Strayer, D. M.; Barner, J. B.; Hunt, B. D.; Foote, M. C.; Vasquez, R. P.; Gupta, A.; Kussmaul, A. Microwave vortex dissipation of superconducting Nd-Ce-Cu-O epitaxial films in high magnetic fields. *Phys. Rev. B* **1993**, *48*, 9861.

(39) Horide, T.; Sakamoto, N.; Ichinose, A.; Otsubo, K.; Kitamura, T.; Matsumoto, K. Hybrid artificial pinning centers of elongated-nanorods and segmented- nanorods in $YBa_2Cu_3O_7$ films. *Supercond. Sci. Technol.* **2016**, *29*, 105010.

(40) Horide, T.; Ishimaru, M.; Matsumoto, K. Observation of inhomogeneous depinning in $YBa_2Cu_3O_7$ composite multilayers. *Supercond. Sci. Technol.* **2019**, *32*, 085001.

(41) Aye, M. M.; Rivasto, E.; Khan, M. Z.; Rijckaert, H.; Palonen, H.; Huhtinen, H.; Van Driessche, I.; Paturi, P. Multilayering BZO nanocolumns with different defect densities for YBCO high field applications. *New J. Phys.* **2021**, *23*, 113031:1–12.

(42) Krusin-Elbaum, L.; Civale, L.; Thompson, J. R.; Feild, C. Accommodation of vortices to columnar defects: Evidence for large entropic reduction of vortex localization. *Phys. Rev. B* **1996**, *53*, 11744–11750.

(43) Cai, C.; Holzapfel, B.; Hänisch, J.; Fernandez, L.; Schultz, L. Magnetotransport and flux pinning characterictics in RBaCuO (R=Gd,Eu,Nd) and $(Gd_{1/3}Eu_{1/3}Nd_{1/3})$BaCuO high-$T_c$ superconducting thin films on $SrTiO_3$. *Phys. Rev. B* **2004**, *69*, 104531:1–8.

(44) Rivasto, E.; Khan, M. Z.; Malmivirta, M.; Rijckaert, H.; Aye, M. M.; Hynninen, T.; Huhtinen, H.; Driessche, I. V.; Paturi, P. Self-assembled nanorods in YBCO matrix – a computational study of their effects on critical current anisotropy. *Sci. Reports* **2020**, *10*, 3169:1–14.

(45) Khan, M. Z.; Rivasto, E.; Rijckaert, H.; Zhao, Y.; Liedke, M. O.; Butterling, M.; Wagner, A.; Van Driessche, I.; Huhtinen, H.; Paturi, P. Strongly Enhanced Growth of High-Temperature Superconducting Films on an Advanced Metallic Template. *Cryst. Growth Des.* **2022**, *22*, 2097–2104.

(46) Maiorov, B.; Baily, S. A.; Zhou, H.; Ugurlu, O.; Kennison, J. A.; Dowden, P. C.; Holesinger, T. G.; Foltyn, S. R.; Civale, L. Synergetic combination of different types of defect to optimize pinning landscape using $BaZrO_3$-doped $YBa_2Cu_3O_7$. *Nat. Mater.* **2009**, *8*, 398–404.

(47) Baca, F. J.; Haugan, T. J.; Barnes, P. N.; Holesinger, T. G.; Maiorov, B.; Lu, R.; Wang, X.; Reichart, J. N.; Wu, J. Z. Interactive Growth Effects of Rare-Earth Nanoparticles on Nanorod Formation in $YBa_2Cu_3O_x$ Thin Films. *Adv. Funct. Mater.* **2013**, *23*, 4826–4831.

(48) Pan, A. V.; Golovchansky, I. A.; Fedoseev, S. A. Critical current density: Measurement vs. reality. *EPL* **2013**, *103*, 17006.

(49) Goyal, A.; Kang, S.; Leonard, K. J.; Martin, P. M.; Gapud, A. A.; Varela, M.; Paranthaman, M.; Ijaduola, A. O.; Specht, E. D.; Thompson, J. R.; Christen, D. K.; Pennycook, S. J.; List, F. A. Title. *Supercond. Sci. Technol.* **2005**, *18*, 1533.

(50) Malmivirta, M.; Yao, L.; Huhtinen, H.; Palonen, H.; van Dijken, S.; Paturi, P. Three ranges of the angular dependence of cirtical current of $BaZrO_3$ doped $YBa_2Cu_3O_{7-\delta}$ thin films grown at different temperatures. *Thin Solid Films* **2014**, *562*, 554–560.

(51) Gapud, A. A.; Kumar, D.; Viswanathan, S. K.; Cantoni, C.; Varela, M.; Abiade, J.; Pennycook, S. J.; Christen, D. K. Enhancement of flux pinning in YBCO thin films embedded with epitaxially grown Y2O3 nanostructures using multi-layering process. *Supercond. Sci. Technol.* **2005**, *18*, 1502.

(52) Develos-Bagarinao, K.; Yamasaki, H.; Ohki, K. Flux pinning properties of YBCO/DyBCO multilayers. *J. Appl. Phys.* **2008**, *104*, 063907.

(53) Cai, C.; Holzapfel, B.; Hänisch, J.; Schultz, L. Superconductivity suppression and flux-pinning crossover in artificial multilayers of ternary $RBa_2Cu_3O_{7-\delta}$ (R = Gd, Nd and Eu). *Phys. Rev. B* **2004**, *70*, 064504.

(54) Paturi, P.; Huhtinen, H. Roles of electron mean free path and flux pinning in optimizing the critical current in YBCO superconductors. *Supercond. Sci. Technol.* **2022**, *35*, 065007:1–9.

(55) Aye, M. M.; Rivasto, E.; Vaimala, T.; Zhao, Y.; Huhtinen, H.; Paturi, P. Improved crystalline quality and self-field J_c in sequentially vacuum-multilayered YBCO thin films on buffered metallic templates. *IEEE T. Appl. Supercond.* **2023**, *33*, 6601806:1–6.

(56) Tuomola, A.; Rivasto, E.; Aye, M. M.; Zhao, Y.; Huhtinen, H.; Paturi, P. Defining optimal thickness for maximal self-field J_c in YBCO/CeO_2 multilayers grown on buffered metal. *J. Phys. Cond. Mat.* **2023**, *35*, 475001:1–9.

(57) Tallon, J. L.; Pooke, D. M.; Staines, M. P.; Bowden, M. E.; Flower, N. E.; Buckley, R. G.; Presland, M. R.; Davis, R. L. Giant enhancement of oxygen mobility in high-T_c superconductors by atomic substitution. *Physica C* **1990**, *171*, 61–68.

(58) Kucera, J. T.; Bravman, J. C. Transport characterization of calcium-doped YBCO thin films. *Phys. Rev. B* **1995**, *51*, 8582–8590.

(59) Zhao, Y.; Liu, H. K.; Dou, S. X. Effect of co-doping of Ca and Al on hole concentration and superconductivity in the YBCO system. *Physica C* **1991**, *179*, 207–213.

(60) Horide, T.; Kametani, F.; Yoshioka, S.; Kitamura, T.; Matsumoto, K. Structural Evolution Induced by Interfacial lattice Mismatch in Self-organized $YBa_2Cu_3O_{7-\Delta}$ Nanocomposite Film. *ACS Nano* **2017**, *11*, 1780–1788.

(61) Schmehl, A.; Goetz, B.; Schulz, R. R.; Schneider, C. W.; Bielefeldt, H.; Hilgenkamp, H.; Mannhart, J. Doping-induced enhancement of the critical currents of grain boundaries in $YBa_2Cu_3O_{7-\delta}$. *Europhysics Letters* **1999**, *47*, 110–115.

(62) Klaassen, F. C.; Doornbos, G.; Huijbregtse, J. M.; van der Geest, R. C. F.; Dam, B.; Griessen, R. Vortex pinning by natural linear defects in thin films of $YBa_2Cu_3O_{7-\delta}$. *Phys. Rev. B* **2001**, *64*, 184523:1–20.

(63) Blatter, G.; Feigel'man, M. V.; Geshkenbein, V. B.; Larkin, A. I.; Vinokur, V. M. Vortices in high-temperature superconductors. *Reviews of Modern Physics* **1994**, *66*, 1125–1388.

(64) Clem, J. R. Simple Model for the Vortex Core in a Type II Superconductor. *J. Low Temp. Phys.* **1975**, *18*, 427.

(65) Poole, C. P.; Farach, H. A.; Creswick, R. J.; Prozorov, R. *Superconductivity*; Amsterdam: Academic Press, 2007.

For Table of Contents Use Only

Enhanced critical current density in heterostructural YBCO/Ca-doped YBCO multilayers

Moe Moe Aye, Elmeri Rivasto, Hannu Huhtinen, and Petriina Paturi

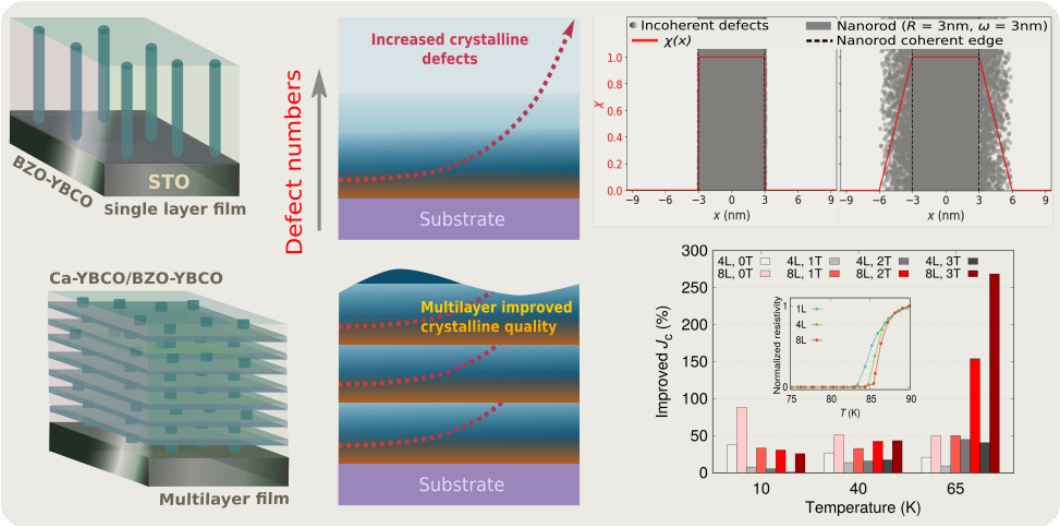

This work investigates how adding Ca-doped YBCO layers to multilayer structures of BZO-added YBCO enhances critical current density (J_c). Experimental findings demonstrate that these Ca-doped layers improve the YBCO matrix quality within the BZO-added layer by reducing microstrain and crystalline defects, while also optimizing oxygen content with increasing layer number. This enhancement significantly boosts self-field $J_c(0)$ and in-field J_c(B) without directly impacting flux pinning, underscoring the crucial role of heterostructures in optimizing the performance of BZO-doped YBCO multilayer films.